A Dedicated Compression Device for High Resolution X-ray Tomography of Compressed Gas Diffusion Layers

C. Tötzke[a, b], I. Manke[b], G. Gaiselmann[c], J. Bohner[d] , B. Müller[e], A. Kupsch[e], M. P. Hentschel[e], V. Schmidt[c], J. Banhart[a] and W. Lehnert [d,f]
[a] Helmholtz Center Berlin for Materials and Energy GmbH, Berlin, 14109, Germany
[b] Institute of Earth and Environmental Science, University of Potsdam, 14476 Potsdam, Germany
[c] Universität Ulm, 89069 Ulm, Germany
[d] Forschungszentrum Jülich, 52428 Jülich, Germany
[e] Bundesanstalt für Materialforschung und –prüfung, 12205 Berlin, Germany
[f]RTWH Aachen, 52062 Aachen, Germany

We present an experimental approach to study the three-dimensional microstructure of GDL materials under realistic compression conditions. A dedicated compression device was designed that allows for synchrotron-tomographic investigation of circular samples under well-defined compression conditions. The tomographic data provides the experimental basis for stochastic modeling of nonwoven GDL materials. A plain compression tool is used study the fiber courses in the material at different compression stages. Transport relevant geometrical parameter, such as porosity, pore size and tortuosity distributions, are exemplarily evaluated for a GDL sample in the uncompressed state and for a compression of 30 vol.%. The influence of the channel rip geometry on the compressed GDL morphology is studied using a compression tool with an integrated channel profile. While the GDL is homogenously compressed under the rips it is much less compressed under the channel where it extends far into the channel confining space for convective gas transport and the removal of liquid water from the cell.

1. Introduction

Efficient water management of proton-exchange fuel cells (PEFCs) relies on favorable conditions for water and media transport within the gas diffusion layers (GDLs) and is essential for good performance and durability of these cells. A GDL must allow for concurrent transfer of gaseous reactants from the flow-field channels to the electrodes and effective removal of liquid product water. Furthermore, the membrane must be kept humidified to maintain its proton conductivity.[1-4] Common GDL types consist of porous carbon fiber-based materials with carefully adjusted water transport and storage capacities. The transport mechanism of two-phase flow in porous media was subject of numerous theoretical[5-9] and experimental[10, 11] studies.

Especially, neutron and X-ray imaging techniques turned out as powerful tools for the investigation of water in porous materials like GDLs.[8, 12-27] As transport properties of GDLs are closely linked with their microstructure precise knowledge of the three-dimensional morphology is the key to understand the functionality of GDLs.[28-30]

A sophisticated way to optimize materials design is to detect microstructures with improved physical properties by means of model-based computer experiments. Appropriate stochastic geometry models are required to create virtual 3-D structures, the corresponding transport properties of which can be evaluated by means of numerical transport simulations. Systematic parameter modification of geometry model along with numerical transport simulation can efficiently assist the identification of suitable transport geometries.[31-33]

We performed high resolution synchrotron X-ray measurements on various GDL materials at different degrees of compression aiming at the generation of a broad tomographic data set that can be used for the development and validation of stochastically derived geometry models.[33]

2. Experimental set-up

Imaging conditions

The synchrotron imaging experiments were performed at the tomography station of the BAMline using the synchrotron which is located at the synchrotron source BESSY II (Helmholtz-Zentrum Berlin /Germany).[34]

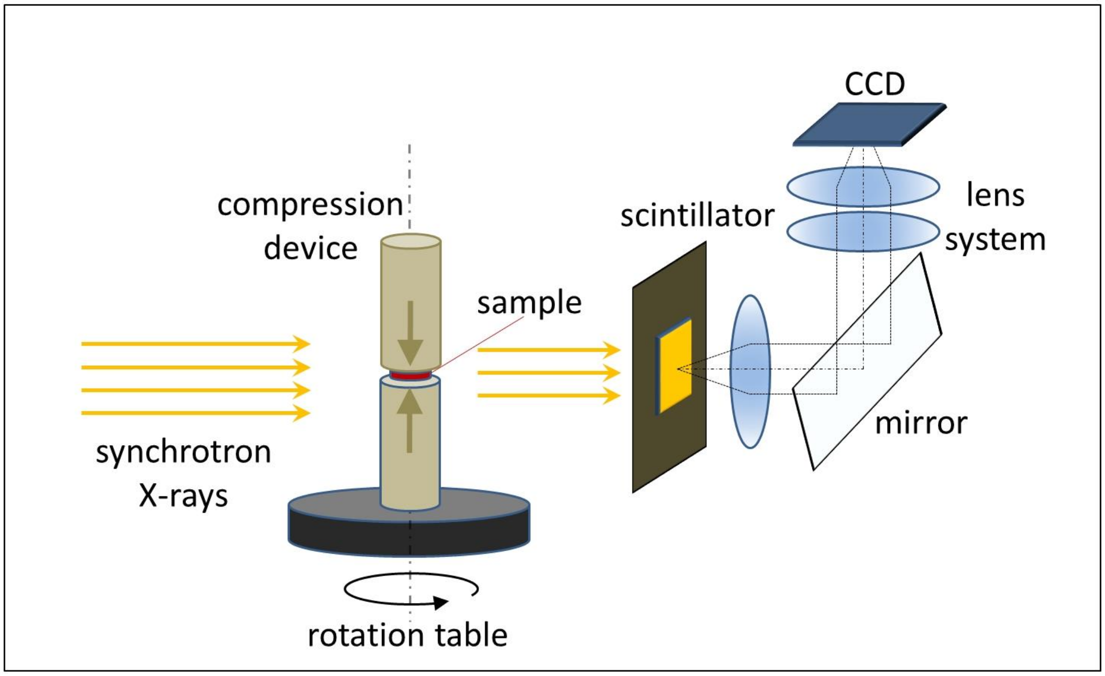

Figure 1. Scheme of the principal experimental set up at the tomographic instrument.

Monochromatic X-rays were generated by means of a W-Si monochromator with an energy resolution of $\Delta E/E=10^{-2}$. In order to achieve optimal contrast for fibers the beam energy was adjusted to 15 keV. We employed an optical system consisting of a PCO camera, a lens system and a Gadox scintillator screen to capture digital images with dimensions of 4008×2672 pixel^2. The pixel size was 0.876 µm which corresponds to a physical spatial resolution of about 2 µm rendering a field of view of 3.3×2.2 mm^2. The principal set up is sketched in figure 1.[35] The sample holder was mounted on a translation/rotation unit. Circular GDL samples with diameters of 3 mm were adjusted. A stepwise rotation over 180° was performed to capture a radiographic set of 1500 projections. In addition, 500 flatfields were taken to normalize the projections. The exposure time for a single radiograph was 2.5 s plus 1.7 s read-out time referring to a total acquisition time of 140 min for the entire tomographic scan. After image normalization the radiographic dataset was reconstructed to a 3D volume.

Sample compression device

The acquisition of highly resolved synchrotron X-ray absorption tomograms of GDL samples under well-defined compression conditions implies some technically demanding design requirements for the sample holder, i.e. the compression device. Planar and horizontal sample alignment facilitates the data analysis: When aligned in planar, horizontal manner, the sample orientation coincides with the reconstructed tomographic slices what has practical advantages for the geometric analysis. Furthermore, the degree of compression, in terms of the reduction of sample volume, must be precisely adjustable by a compression punch. Therefore, the position of this punch should be controlled with an accuracy of a few micrometers. In order study different compression patterns it should be possible to install differently shaped compression punches. A plain punch is sufficient to realize homogenous compression condition while a channel profile (see figure 2B right) is required to mimic compression conditions of assembled fuel cells, where the mechanical interaction of GDL and flow-field gives rise for an embossed channel-rip-pattern. Also requirements of the imaging instruments have to be taken into account. The most important points are sufficient beam transmission and dimensional restrictions with regard to the small field of view which is usually a view millimeters at a resolution of 1 µm. Moreover, the stability of the construction must be appropriate to keep the sample at rest during tomographic scans. Thermal material expansion caused by the energy input of the incident beam should be as small as possible as it could easily influence the sample position within the µm-range.

A dedicated compression device that can cope with these technical challenges was designed and manufactured by Forschungszentrum Jülich.

Figure 2 illustrates the principal design of the compression device which basically consists of the sample bearing base part (figure 2 C left) and the compression unit fastened on top. This unit is build up as follows: a metal sleeve (figure 2 D right) with a female ultra-fine thread is screwed into the polyimide casing. The compression punch positioned beneath travels downward when the adjustment screw is fastened (figure 2 D left). When unscrewing it the punch is returned by a retaining spring. A mounting pin guided in a groove of the polyimide casing prevents any rotation of the travelling punch to ensure a torsion-free sample compression.

The design of the compression device facilitates quick and easy exchange of samples which helps to save valuable beam time at the electron storage ring. After the compression unit has been unfastened the sample can be mounted on the top plateau of the base part.

Figure 2. Compression device used for high resolution tomography of circular GDL samples. A: total view. B: transparent total view revealing interior details of the construction. C: Sample holder basis (left) and compression punch with integrated channel structure mimicking the flow field channel geometry (right). D: Hollow adjustment screw and sleeve made of brass. E: Detail of the adjustment screw showing the male ultra-fine thread (pitch = 200 µm).

Subsequently, the compression unit is refastened and the punch can be settled. As the pitch of the setting screw is 200 µm a full screw rotation will drive the punch 200 µm downwards. When approaching the sample in smaller steps it is possible to adjust punch position and, hence, the sample thickness very precisely. For this, the relative position of the punch can be checked with a scale reading while its absolute position is double-checked radiographically by the CCD camera. Figure 3 demonstrates that the punch position can be adjusted with a precision of about ± 5 µm when approaching the sample step by step with increments no larger than half of a screw rotation.

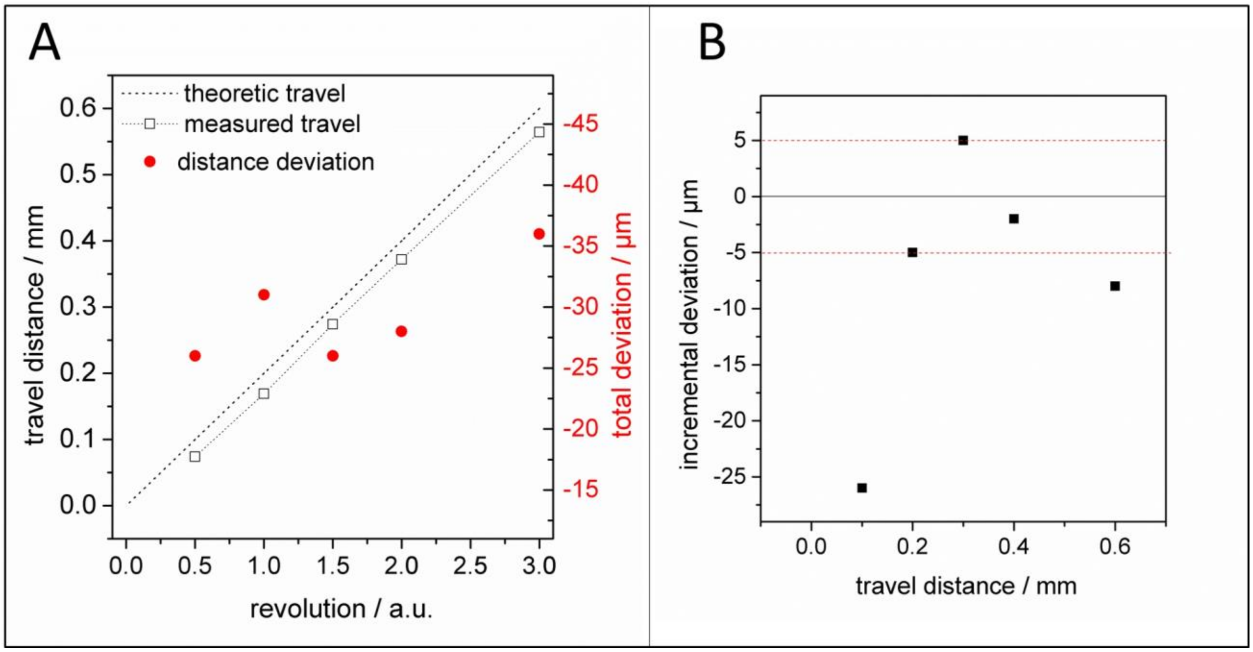

Figure 3. Positioning accuracy of the compression punch. A. travel distance of compression punch plotted as function of setting screw rotation. Theoretic travel as given by the thread pitch. B. Incremental deviation for the stepwise travel of the punch. First measure point (at 0.1mm) reflects the free play of the punch – setting screw connection. Position accuracy of ± 5 µm can be achieved for position steps < 0.1 mm or ½ screw rotation (see text).

The casing of the compression device is made of durable high-performance polyimide-based polymer (Vespel®). Within the field of view its wall thickness has been reduced to 1mm to achieve high beam transmission. The compression unit can be assembled with different compression tools: a planar punch to realize a homogenous compression and a punch with integrated channel profile (0.8 mm wide and 1 mm deep) (see figure 2 B, right). The maximum possible pressure of the device is limited to about 1-3 MPa, i.e. the device is optimized for soft materials and not suited for hard materials like rocks or metals.[36] A summary of some important parameters of the device can be found in table 1

Table 1: Some important parameters of the compression device.

sample size	max. diameter = 3 mm
max. diameter of device	28 mm
field of view (X-rays)	4.4 mm x 2.9 mm
precision of compression	± 5 µm
channel profile width/heigth	0.8 mm / 1 mm

max. clamping pressure	1-3 MPa
operating temperature	20-50 °C
material	Vespel SP-1

3. Results and discussion

The present tomographic study covers a range of different GDL materials measured at four stages of increasing compression (0, 10, 20, and 30 vol. %). In this paper, we exemplarily show results for morphology of the material type H2315 (manufactured by Freudenberg FCCT) in the uncompressed state and compressed by 30% of initial volume. This material represents a standard nonwoven GDL material without water proofing additives or binder. Figure 4 shows half of the reconstructed volume of the same sample in the uncompressed and compressed state. The sample was virtually cut to show a cross section of the material. The initial GDL thickness of about 220 µm is reduced by 30% to a value of 176 µm. The thickness reduction of the sample did not result in a significant lateral expansion, i.e. no significant diameter extension was observed. This suggests that mainly the pore space was compressed. Upon reconstruction the sample volume was binarized employing a global threshold to separate pore space from the solid phase (fibers).

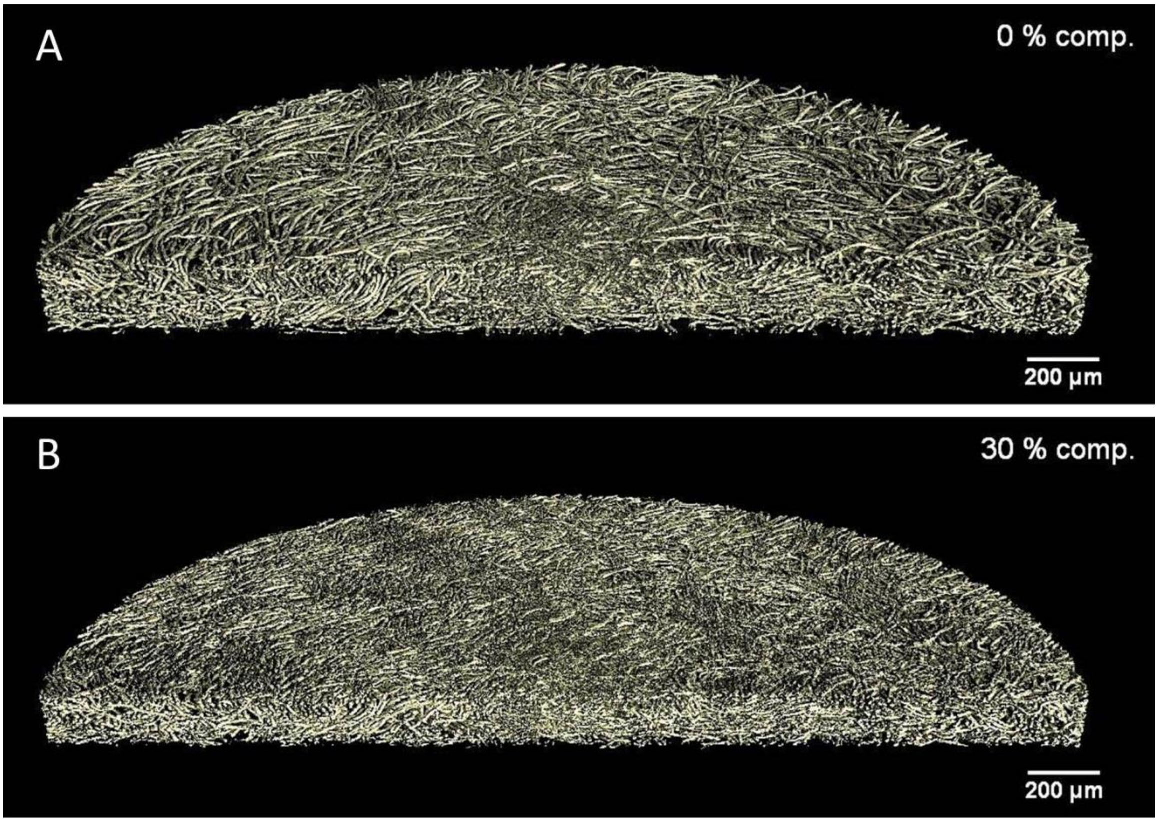

Figure 4. 3D representation of an A: uncompressed and B: compressed GDL sample (by 30 vol. %) (Type Freudenberg H2315).

In order to analyze the influence of compression on the microstructure several structural characteristics are calculated and compared to each other for uncompressed and 30% compressed GDL, respectively. First the porosity and the specific surface area are stated in Table 2.

Table 2: Porosity and mean geometric tortuosity computed for the uncompressed and compressed GDL

Compression	Porosity	Mean tortuosity	Standard deviation (tortuosity)
0 vol.%	0.78	1.50	0.099
30 vol.%	0.67	1.48	0.092

Subsequently, the spherical contact distribution functions $H : [0, \infty) \rightarrow [0, 1]$ from background (pore) to foreground (solid) phase is computed, where $H(t)$ is the probability that the minimum distance from a randomly chosen point of the pore phase to the solid phase is not larger than $t > 0$. As further structural characteristic, the continuous pore size distribution $[0, \infty) \rightarrow [0, 1]$ has been calculated for the uncompressed and compressed GDL, where $P(t)$ is the volume fraction, which can be covered by spheres with center belonging to the pore phase, and radius t, such that these spheres have no intersection with the foreground phase, see Münch et al.[37] The results are displayed in figure 5.

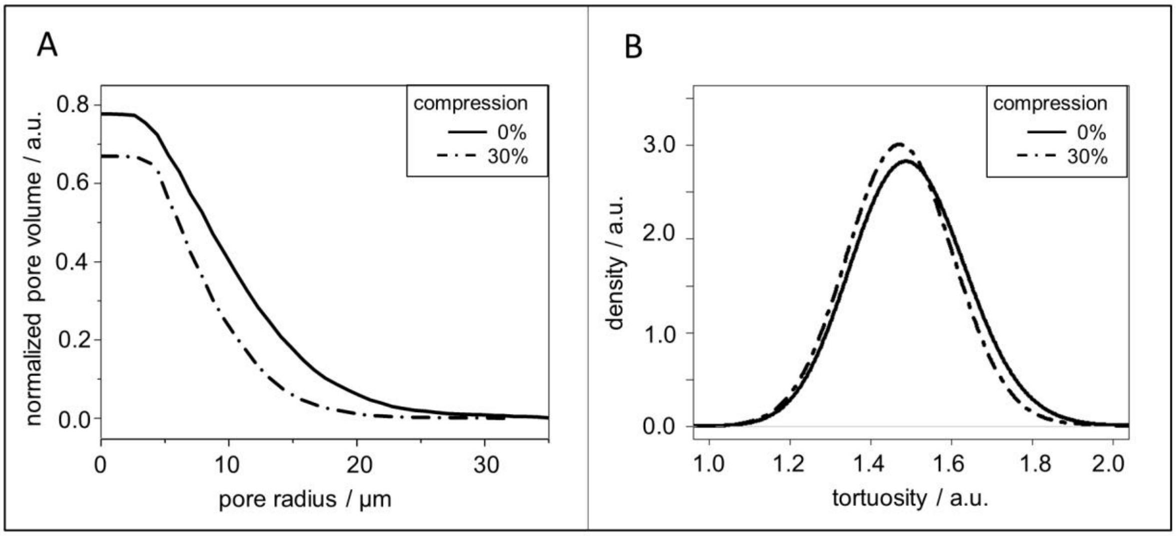

Figure 5. A: Continues pore size distribution (cPSD); B: distribution of geometric tortuosity P (right) computed for uncompressed and compressed state

Furthermore, for the porous material considered in the present paper, the geometrical properties of the percolation pathways through the pore phase play an important role for the transport of gas-molecules within the GDL. Therefore, we investigated the 'geometric tortuosity' of the pore space, which is defined as the Euclidean length of shortest paths along the edges of a geometric 3D graph representing the possible paths through the pore phase divided by the material thickness. Note that starting from a randomly chosen location on top of the porous material, its geometric tortuosity can be represented by a probability distribution instead of looking at the mean tortuosity only, see e.g. Thiedmann et al.[38] The geometric 3D graph of the pore phase is computed by means of the skeletonization algorithm implemented in software Avizo 7. The results are given in table 2 and fig. 6a.

In addition to the demonstrated impact of homogenous compression on transport-relevant geometric parameter of the GDL microstructure we have also simulated the effect of inhomogeneous compression caused by the mechanical interaction of the GDL with the channel rip pattern of the flow-field. We used the compression tool with the integrated channel profile to simulate the influence of the flow-field geometry to compress the GDL by 30% of its initial thickness. Figure 6shows a perspective view on the GDL sample that was compressed. The sample was virtually cut to provide a cross sectional insight. The visualization of the reconstructed volume shows nicely that the shape of the compressing tool is stamped into the GDL sample generating considerable differences in the local material density. While the GDL under the rips is homogenously compressed to the thickness determined by the compression tool the GDL fiber structure is much less compressed below the channel. Along the center line of the channel the GDL thickness almost remains unaltered. Consequently, when assembled in fuel cells, the GDL material significantly extends into the channel volume where it exerts influence on the media flow. Figure 6 also documents that some individual fiber endings are erected by the bending stress exerted by the channel edge. This fiber end may have a significant influence on the gas flow profile inside the channel and could alter the flow regime, e.g. by producing vortexes.

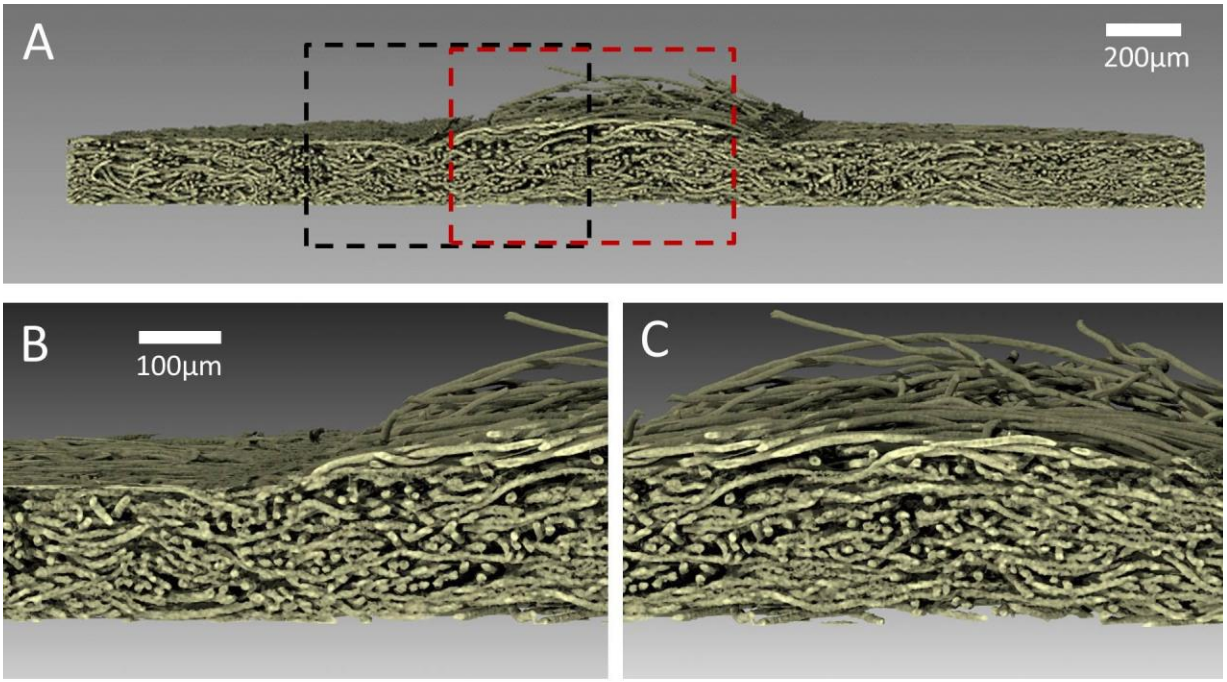

Figure 6. A: 3D rendering of a compressed GDL demonstrating the inhomogeneous compression caused by the channel-rip pattern of the flow-field. B: transition zone between channel rip area. C. GDL structure underneath the channel.

Figures 6 B and C shows that the characterization of the microstructure in terms of the transport relevant geometric parameters requires a partition in sub-areas according to the relative position with respect to the channel-rip-pattern of the flow-field. While the areas underneath rips can be handled equivalently to the case of a homogenously compressed GDL the local geometric parameters within the transition zone along the channel edges vary strongly (see figure 6 B).

4. Conclusion and Outlook

Synchrotron X-ray tomography was demonstrated to be a powerful tool to analyze the microstructure of porous fiber-based materials such as nonwoven GDL. Taking advantage of dedicated compression device highly resolved tomographic data of compressed GDL morphologies can be produced.[33] This data is used for geometric analysis of transport relevant structure parameter and serves as experimental basis to develop mathematical structure models.[32] This approach paves the way for virtual material design, i.e. the generation of virtual GDL structures with optimized physical properties.

References

1. C.-Y. Wang, Chemical Reviews **104** (10), 4727-4766 (2004).
2. W. Vielstich, A. Lamm and H. A. Gasteiger, (John Wiley & Sons, Chichester, 2003), Vol. 3.
3. L. Carrette, K. A. Friedrich and U. Stimming, Fuel Cells **1** (1), 5-39 (2001).
4. J. R. Bunn, D. Penumadu, R. Woracek, N. Kardjilov, A. Hilger, I. Manke and S. Williams, Applied Physics Letters **102** (23), 234102 (2013).
5. U. Pasaogullari and C.-Y. Wang, Journal of The Electrochemical Society **152** (2), A380-A390 (2005).
6. C. Ziegler, H. M. Yu and J. O. Schumacher, Journal of The Electrochemical Society **152** (8), A1555-A1567 (2005).
7. C. Y. Wang and P. Cheng, International Journal of Heat and Mass Transfer **39** (17), 3607-3618 (1996).
8. P. K. Sinha, P. P. Mukherjee and C. Y. Wang, Journal of Materials Chemistry **17**, 3089-3103 (2007).
9. P. Zhou and C. W. Wu, Journal of Power Sources **195**, 1408-1415 (2010).
10. A. Bazylak, D. Sinton and N. Djilali, Journal of Power Sources **176** (1), 240-246 (2008).
11. S. Litster, D. Sinton and N. Djilali, Journal of Power Sources **154** (1), 95-105 (2006).
12. R. J. Bellows, M. Y. Lin, M. Arif, A. K. Thompson and D. Jacobson, Journal of The Electrochemical Society **146** (3), 1099 - 1103 (1999).
13. R. Satija, D. L. Jacobson, M. Arif and S. A. Werner, Journal of Power Sources **129** (2), 238-245 (2004).
14. M. A. Hickner, N. P. Siegel, K. S. Chen, D. S. Hussey, D. L. Jacobson and M. Arif, Journal of The Electrochemical Society **155** (4), B427-B434 (2008).
15. A. B. Geiger, A. Tsukada, E. Lehmann, P. Vontobel, A. Wokaun and G. G. Scherer, Fuel Cells **2** (2), 92-98 (2002).
16. P. Boillat, G. Frei, E. H. Lehmann, G. G. Scherer and A. Wokaun, Electrochemical and Solid-State Letters **13** (3), B25-B27 (2010).
17. N. Pekula, K. Heller, P. A. Chuang, A. Turhan, M. M. Mench, J. S. Brenizer and K. Ünlü, Nuclear Instruments and Methods in Physics Research Section A: Accelerators, Spectrometers, Detectors and Associated Equipment **542** (1-3), 134-141 (2005).
18. P. K. Sinha, P. Halleck and C.-Y. Wang, Electrochemical and Solid-State Letters **9** (7), A344-A348 (2006).
19. I. Manke, C. Hartnig, M. Grunerbel, W. Lehnert, N. Kardjilov, A. Haibel, A. Hilger, J. Banhart and H. Riesemeier, Applied Physics Letters **90** (17), 174105 (2007).
20. C. Hartnig, I. Manke, J. Schloesser, P. Krüger, R. Kuhn, H. Riesemeier, K. Wippermann and J. Banhart, Electrochemistry Communications **11** (8), 1559-1562 (2009).
21. C. Totzke, I. Manke, A. Hilger, G. Choinka, N. Kardjilov, T. Arlt, H. Markotter, A. Schroder, K. Wippermann, D. Stolten, C. Hartnig, P. Kruger, R. Kuhn and J. Banhart, Journal of Power Sources **196** (10), 4631-4637 (2011).
22. S. R. Stock, .International Materials Reviews **53**, 129-181 (2008).
23. R. Kuhn, J. Scholta, P. Krueger, C. Hartnig, W. Lehnert, T. Arlt and I. Manke, Journal of Power Sources **196** (12), 5231-5239 (2011).
24. W. Maier, T. Arlt, C. Wannek, I. Manke, H. Riesemeier, P. Krüger, J. Scholta, W. Lehnert, J. Banhart and

D. Stolten, Electrochemistry Communications **12** (10), 1436-1438 (2010).

25. A. Schröder, K. Wippermann, J. Mergel, W. Lehnert, D. Stolten, T. Sanders, T. Baumhöfer, D. U. Sauer, I. Manke, N. Kardjilov, A. Hilger, J. Schloesser, J. Banhart and C. Hartnig, Electrochemistry Communications **11** (8), 1606-1609 (2009).
26. A. Lange, A. Kupsch, M. P. Hentschel, I. Manke, N. Kardjilov, T. Arlt and R. Grothausmann, Journal of Power Sources **196** (12), 5293-5298 (2010).
27. H. Markotter, J. Haussmann, R. Alink, C. Totzke, T. Arlt, M. Klages, H. Riesemeier, J. Scholta, D. Gerteisen, J. Banhart and I. Manke, Electrochemistry Communications **34**, 22-24 (2013).
28. H. Markötter, I. Manke, P. Krüger, T. Arlt, J. Haussmann, M. Klages, H. Riesemeier, C. Hartnig, J. Scholta and J. Banhart, Electrochemistry Communications **13** (9), 1001-1004 (2011).
29. H. Markotter, R. Alink, J. Haussmann, K. Dittmann, T. Arlt, F. Wieder, C. Totzke, M. Klages, C. Reiter, H. Riesemeier, J. Scholta, D. Gerteisen, J. Banhart and I. Manke, International Journal of Hydrogen Energy **37** (9), 7757-7761 (2012).
30. R. Alink, J. Haußmann, H. Markötter, M. Schwager, I. Manke and D. Gerteisen, Journal of Power Sources **233** (0), 358-368 (2013).
31. G. Gaiselmann, D. Froning, C. Tötzke, C. Quick, I. Manke, W. Lehnert and V. Schmidt, Journal of Materials Science (2012, submitted).
32. G. Gaiselmann, C. Tötzke, I. Manke, W. Lehnert and V. Schmidt, Journal of Power Sources **257** (0), 52-64 (2014).
33. C. Tötzke, G. Gaiselmann, M. Osenberg, J. Bohner, T. Arlt, H. Markötter, A. Hilger, F. Wieder, A. Kupsch, B. R. Müller, M. P. Hentschel, J. Banhart, V. Schmidt, W. Lehnert and I. Manke, Journal of Power Sources **253** (0), 123-131 (2014).
34. W. Görner, M. P. Hentschel, B. R. Müller, H. Riesemeier, M. Krumrey, G. Ulm, W. Diete, U. Klein and R. Frahm, Nuclear Instruments and Methods in Physics Research Section A: Accelerators, Spectrometers, Detectors and Associated Equipment **467-468** (Part 1), 703-706 (2001).
35. S. H. Williams, A. Hilger, N. Kardjilov, I. Manke, M. Strobl, P. A. Douissard, T. Martin, H. Riesemeier and J. Banhart, Journal of Instrumentation **7**, P02014 (2012).
36. S. Zabler, A. Rack, I. Manke, K. Thermann, J. Tiedemann, N. Harthill and H. Riesemeier, Journal of Structural Geology **30** (7), 876-887 (2008).
37. B. Münch and L. Holzer, Journal of the American Ceramic Society **91** (12), 4059-4067 (2008).
38. R. Thiedmann, C. Hartnig, I. Manke, V. Schmidt and W. Lehnert, Journal of the Electrochemical Society **156** (11), B1339-B1347 (2009).